Wind Power Applications of Doubly-Fed Reluctance Generators with Parameter-Free Hysteresis Control

Milutin Jovanović[a,*], Hamza Chaal[b]

[a] *Faculty of Engineering and Environment, Department of Physics and Electrical Engineering Northumbria University Newcastle, Newcastle upon Tyne NE1 8ST, UK*

[b] *Siemens plc, Renewable Energy Division, Keele ST5 5NP, UK*

Abstract

The development and practical implementation aspects of a novel scheme for fast power control of the doubly-fed reluctance generator with a low-cost partially-rated converter, a promising brushless candidate for limited speed ranges of wind turbines, are presented in this paper. The proposed concept is derived from the fundamental dynamic analogies between the controllable and measurable properties of the machine: electro-magnetic torque and electrical power, and flux and reactive power. The algorithm is applied in a stationary reference frame without any knowledge of the machine parameters, including rotor angular position or velocity. It is then structurally simpler, easier to realise in real-time and more tolerant of the system operating uncertainties than model-based or proportional-integral control alternatives. Experimental results have demonstrated the excellent controller response for a variety of speed, load and/or power factor states of a custom-built generator prototype.

Keywords: Reactive power control, Sensorless power regulation, Doubly-fed machines, Reluctance generators, Wind turbines.

*Corresponding author

Nomenclature

$v_{p,s}$	primary, secondary winding phase voltages [V]
$e_{p,s}$	primary, secondary winding back-emf [V]
$i_{p,s}$	primary, secondary winding currents [A]
$R_{p,s}$	primary, secondary winding resistances [Ω]
$L_{p,s}$	primary, secondary 3-phase self-inductances [H]
L_m	3-phase mutual inductance [H]
σ	leakage factor (constant) $= 1 - L_m^2/(L_p L_s)$
$\lambda_{p,s}$	primary, secondary winding flux linkages [Wb]
λ_m	mutual flux [Wb]
$\theta_{p,s}$	primary, secondary flux vector angular positions [rad]
$\omega_{p,s}$	primary, secondary winding frequencies [rad/s]
p, q	primary, secondary winding pole-pairs
p_r	number of rotor poles $= p + q$
ω_{rm}	rotor angular velocity $= d\theta_{rm}/dt$ [rad/s]
θ_r	rotor 'electrical' angular position $= p_r\theta_{rm}$ [rad]
ω_{syn}	synchronous speed $= \omega_p/p_r$ [rad/s]
P_m	total mechanical (shaft) power [W]
$P_{p,s}$	primary, secondary mechanical power [W]
T_e	machine electro-magnetic torque [Nm]
P, Q	primary real [W] and reactive [VAr] power

1. Introduction

A brushless doubly-fed generator (BDFG) may be an attractive solution to reliability and maintenance issues of carbon brushes and slip-rings with a conventional doubly-excited induction generator (DFIG) while offering competitive performance and the same economic benefits of partial power electronics [1]. For a typical speed ratio of 2:1 in wind energy conversion systems (WECS), the converter derating can be about 75% of the machine itself [2]. In this sense, both the BDFG and DFIG are preferable to heavy and expensive multi-pole wound rotor synchronous generators (SGs) or permanent-magnet generators (PMGs) with fully-rated converters, which are not only costly but more prone to failures undermining the otherwise high reliability of their dedicated wind turbines, gear-less technologies in particular [3]. Another concern for the manufacturers of large PMG units is the risk management of market volatility, availability and payable price premiums of the rare earth magnets (e.g. NdFeB) deployed [4].

With the increasing penetration of distributed generation, the challenging requirements have been imposed by the grid integration codes for the reactive (and real) power support to be provided by WECS to help preserve the transient stability during network disturbances (e.g. voltage sags) [5]. Putting these preventive measures in place has revealed another important BDFG potential, the superior low-voltage-ride-through (LVRT) characteristics owing to the inherently higher impedances and thus lower fault currents relative to the equivalent DFIG [6]. This salient BDFG property could facilitate to a great deal the design of hardware and software protection for the LVRT compliant fractionally-rated converter, decreasing so the supplementary system complexity and cost of DFIG installations [7]. DFIG turbines are known to have LVRT weaknesses and many interesting solutions have been recently proposed to find improvements [8]. The latest rigorous review of the extensive research done on this subject has been published in [9]. However, tangible practical advances are yet to be made in this direction for the DFIG to become comparable to the PMG, which is amenable to fulfilling the LVRT obligations due to the use of a full-power converter and favorable low voltage capability curves as demonstrated by the WECS field tests presented in [10].

In order to eliminate brushes for reliable and maintenance-free operation, the BDFG has evolved as a self-cascaded inside-out version of the DFIG [11]. This means that the rotor (secondary or control) winding, usually fed from two standard IGBT bridges in bi-directional ('back-to-back') arrangement to allow both super and sub-synchronous speeds in either machine mode, has been moved to the stator and placed together with the grid-connected (primary or power) winding but of different pole number (Fig. 1). The necessary magnetic interaction between the two windings for the torque production is achieved through the rotor with half the total number of the stator poles [12]. Therefore, for the same number of rotor poles and a given line frequency, the DFIG synchronous speed would be twice that of the BDFG making it naturally a medium-speed machine and avoiding the need for a high-speed gear stage of the vulnerable 3-stage gearbox in WECS [1]. From this point of view, the BDFG could bring higher efficiency and reliability as well as running costs savings in these applications, and especially off-shore [13].

The BDFG reluctance rotor type, the Brushless Doubly-Fed Reluctance Generator (BDFRG in Fig. 1), has several advantages over its 'nested' cage counterpart, the Brushless Doubly-Fed Induction Generator (BDFIG) [12]. Experiments have shown that the BDFRG can be more efficient than the BDFIG of the same stator frame [14]. In addition, the cage-less rotor allows the fewer parameter

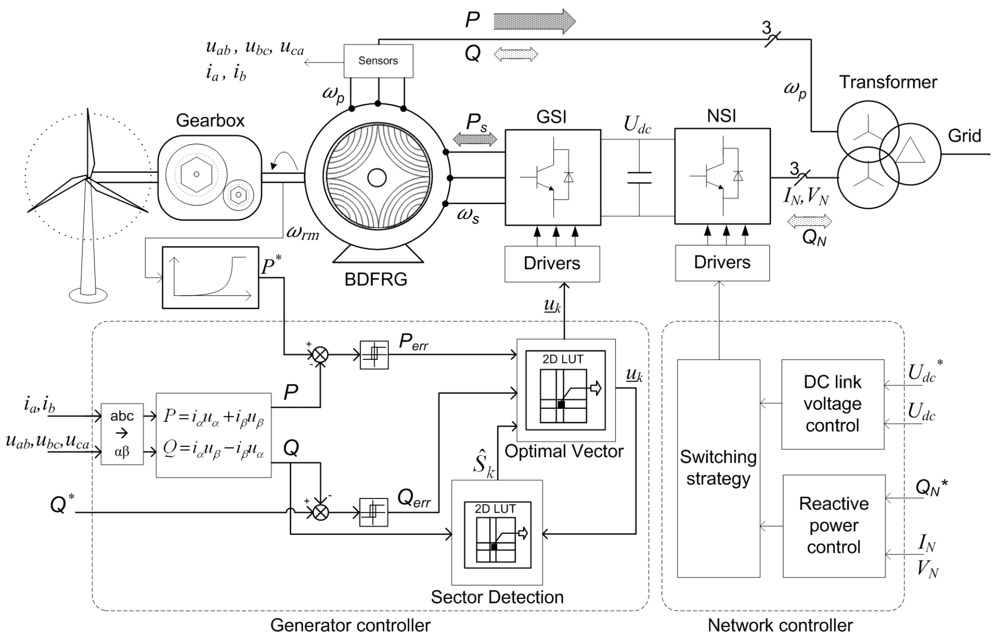

Figure 1: A simplified structural diagram of the BDFRG wind turbine with maximum power point tracking and sensorless hysteresis primary power control of the generator side inverter (GSI).

dependent dynamic modeling, and intrinsically decoupled control of torque and primary reactive power of the BDFRG, unlike the BDFIG [15]. Similar BDFRG attributes are shared by the DFIG [16]. In contrast with the BDFRG or DFIG, the BDFIG has fairly complicated and heavily parameter sensitive model-based vector control [17]. Severe robustness compromises can be affiliated with direct torque controllers for this machine as well [18].

Several 6/2-pole BDFRGs in a kW range have been built, one of which rated at 1.5 kW considered in this paper, and the other to note being a 4 kW counterpart reported in [19]. The more sizeable example recorded in the open literature is a 16 kW, 8/4-pole [12]. One should also mention a 42 kW, 6/2-pole machine studied in [20]. The biggest prototype made so far seems to be a 6/4-pole, 100 kW [21]. An original 2 MW, 6/2-pole design for wind turbines has also been proposed [22].

Research paths on control of other machines have been largely pursued in the BDFRG case over the last decade or so. Although intellectually appealing, the non-linear sliding mode control theory developed in [23] has not been applied in practice to be able to judge on its viability. On the other hand, a stator frame executed direct torque control (DTC) algorithm has been experimentally verified using a shaft position sensor to generate the speed feedback in [24]. This concept has been adapted for sensorless implementation described in [25]. In the underlying DTC approach, the secondary flux is estimated indirectly from the measured primary voltages and currents at fixed line frequency by virtue of the machine double feeding. The back-emf integration errors (e.g. the integrator saturation) caused by the troublesome resistive effects at low inverter voltages and frequencies, as with the traditional DTC of cage induction motors, have been circumvented but at the expense of conspicuous estimation sensitivity to the BDFRG inductance inaccuracies and unsatisfactory performance even for an unloaded machine.

A better quality response can be attained by the weakly parameter dependent modification of DTC, simulated and experimentally validated in [19]. Further test outcomes using the same scheme have been produced in [26]. The practical studies of the direct power control (DPC) correlative have appeared in [27]. However, these improved 'direct' control methods rely on the primary flux estimates and have to face inevitable phase delays and other difficulties commonly associated with filtering noise and transducers DC offset in measurements. Consequently, preliminary no-load results have been mainly shown in all these works.

A thorough comparative analysis of vector control (VC) with primary voltage space vector orientation (VOC) and Field (Flux) Oriented Control (FOC) for various loading profiles in motoring mode (BDFRM) has been done experimentally, and by simulations for the BDFRG, in [28]. The latter have been fully laboratory demonstrated in [29]. The disturbance rejection abilities of the BDFRG controller(s) have been further explored in [30]. Realistic computer simulation studies but on a large-scale WECS level have been presented in [31]. The 2 MW BDFRG design parameters from [22] have been used for this VOC vs FOC performance comparison. Such VC algorithms offer constant and reduced switching rates entailing generally lower harmonic content, but these preferences over the DT(P)C may be often undermined by the tuning problems of multiple PI gains with load, speed and/or machine parameter variations. Besides, an encoder is required for current control in a rotating frame, even though purely sensorless FOC is feasible as documented in [32] using the maximum torque per inverter ampere objective. The encoder-less BDFRG operation under power factor FOC conditions, as an extension of this experimental VC research, has been elaborated in [33].

The hysteresis real and reactive power control (HPQC) strategy put forward in this paper can overcome most of the previously addressed shortcomings of the concurrent torque and/or power control methodologies for the BDFRG. As the name implies, the underlying idea is to govern the accessible terminal quantities rather than electro-magnetic torque and/or flux, which are internal to the machine and susceptible to estimation errors. The obvious advantages over the DTC gained in this way are the algorithm simplicity and higher accuracy, the potential downside being the drive train speed oscillations that may occur in the lack of immediate torque regulation with large wind turbines [2]. Furthermore, unlike the DT(P)C methods discussed earlier, the total parameter-freedom (i.e. an exclusive reliance on measurements, and not estimates) makes the HPQC more robust, simpler and faster to execute. It is also easier to implement than the VC by the absence of PI tuning and intrinsic immunity to parameter uncertainties.

2. Background theory

The space-vector model of the $p$rimary and $s$econdary windings in a stator $\alpha - \beta$ frame (Fig. 2) with standard notation and adopting $motoring$ (BDFRM) convention can be represented as [34]:

$$\left.\begin{aligned} \underline{e}_p = \tfrac{d\underline{\lambda}_p}{dt} = \underline{u}_p - R_p \underline{i}_p = \tfrac{d\lambda_p}{dt} e^{j\theta_p} + j\omega_p \underline{\lambda}_p \\ \underline{e}_s = \tfrac{d\underline{\lambda}_s}{dt} = \underline{u}_s - R_s \underline{i}_s = \tfrac{d\lambda_s}{dt} e^{j\theta_s} + j\omega_s \underline{\lambda}_s \\ \underline{\lambda}_p = \lambda_p e^{j\theta_p} = L_p \underline{i}_p + L_m \underline{i}_s^* e^{j\theta_r} = L_p \underline{i}_p + L_m \underline{i}_{sm}^* \\ \underline{\lambda}_s = \lambda_s e^{j\theta_s} = L_s \underline{i}_s + L_m \underline{i}_p^* e^{j\theta_r} = L_s \underline{i}_s + L_m \underline{i}_{pm}^* \end{aligned}\right\} \quad (1)$$

where $\underline{i}_{pm}$ and $\underline{i}_{sm}$ are the magnetically coupled (magnetizing) current vectors which come from the actual primary ($\underline{i}_p$) and secondary ($\underline{i}_s$) current counterparts rotating at different velocities as shown in Fig. 2. This peculiar frequency modulation through the rotor is hidden in the $e^{j\theta_r}$ term in (1). Note from Fig. 2 that $\underline{i}_{pm} = \underline{i}_p = i_p e^{j\varepsilon}$ and $\underline{i}_{sm} = \underline{i}_s = i_s e^{j\gamma}$ in the corresponding frames [35].

The electro-mechanical energy conversion in the machine takes places under the following angular velocity and pole conditions with the mechanical power relationships showing contributions of each winding [35]:

$$\omega_{rm} = \frac{\omega_p + \omega_s}{p+q} = (1 + \frac{\omega_s}{\omega_p}) \cdot \frac{\omega_p}{p_r} = (1 + \frac{\omega_s}{\omega_p}) \cdot \omega_{syn} \quad (2)$$

$$P_m = T_e \cdot \omega_{rm} = \frac{T_e \cdot \omega_p}{p_r} + \frac{T_e \cdot \omega_s}{p_r} = P_p + P_s \quad (3)$$

where $\omega_s > 0$ for super-synchronous operation ($\omega_{rm} > \omega_{syn}$), $\omega_s < 0$ at sub-

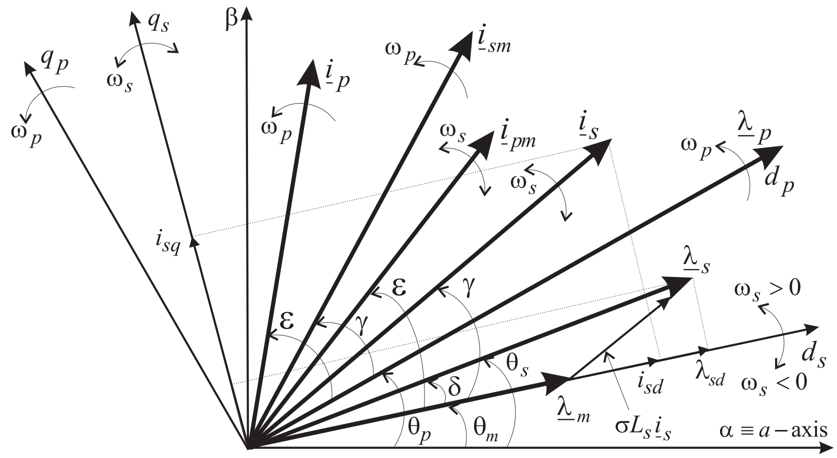

Figure 2: Characteristic space vectors and flux-oriented reference frames.

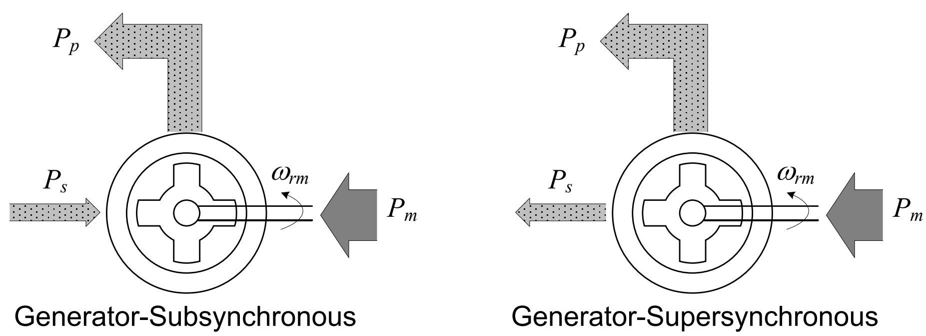

Figure 3: Reference (positive) power flow in the BDFRG for the two speed modes.

synchronous speeds[1]($\omega_{rm} < \omega_{syn}$), and $\omega_s = 0$ (i.e. DC secondary winding) in synchronous speed mode ($\omega_{rm} = \omega_{syn}$) as with a classical $2p_r$-pole wound field turbo-machine. A power flow diagram conforming to (3) appears in Fig. 3.

[1]The 'negative' frequency in this speed region simply means the opposite phase sequence of the secondary to the primary winding i.e. 'clockwise' rotation of the respective vectors in the $d_s - q_s$ frame as indicated in Fig. 2.

3. Principles and architecture of hysteresis control

Using (3), the primary electrical power can be approximated as [24]:

$$P \approx P_p = \underbrace{\frac{3p_r}{2\sigma L_s} \left|\underline{\lambda}_m \times \underline{\lambda}_s\right|}_{T_e} \cdot \frac{\omega_p}{p_r} = \frac{3\omega_p}{2\sigma L_s} \underbrace{\frac{L_m}{L_p} \lambda_p}_{\lambda_m} \lambda_s \sin\delta \tag{4}$$

where λ_p, and thus λ_m, amplitudes are almost constant because of the primary winding grid connection. The real power can therefore be controlled in a stationary frame through $\underline{\lambda}_s$ angle, θ_s, i.e. $\delta = \theta_s - \theta_m$ (Fig. 2) in a DTC fashion as slowly ω_s varying θ_m can hardly change during a short control interval [24].

The Q control notion has been deduced from the fact that the two windings jointly participate in the production of the nearly fixed air-gap flux in the BDFRG. So, if one winding subsidizes more, the other should commit less in the flux build-up. Since the electro-magnetic phenomena are strongly linked with the magnetizing currents, and hence the respective flux values, one can map the primary Q variations with those on the controllable secondary side in the sense that Q increase/decrease could be obtained by reducing/increasing the λ_s. These intuitive hypotheses are easiest to prove mathematically using the Q expression that can be derived from the steady-state FOC form of (1) [30]:

$$Q = \frac{3}{2}\omega_p \left(\frac{\lambda_p^2}{L_p} - \lambda_m i_{sd} \right) = \frac{3e_p}{2L_p} (\lambda_p - L_m i_{sd}) \tag{5}$$

where $e_p = \omega_p \lambda_p \approx u_p$. Given that $\lambda_p \approx const$, the higher Q from the grid, the lower i_{sd}, and thus i_s, and vice-versa. Since $\sigma L_s i_s$ has qualitatively the same trend as i_s does, so will λ_s in keeping with the phasor diagram in Fig. 2.

3.1. Inverter voltages and power implications

The usual binary representations of the inverter legs switching status for the six active voltage vectors ($\underline{u}_k$), where k denotes the attributed sector number (e.g. $\underline{u}_1 \equiv 100$, $\underline{u}_2 \equiv 110$ etc.), are illustrated in Fig. 4. It has been shown in [24] that the other two zero-vectors (e.g. '111' and '000') have contradictory influences on T_e and λ_s behavior above and below the synchronous speed (ω_{syn}). The same holds true for their dual quantities, P and Q, which are control variables here. So, precise speed sensing or estimation is imperative in this case, and especially near or at ω_{syn} where the BDFRG is normally operated anyway. Needless to say that this would complicate the HPQC design and implementation. Another serious challenge in this speed region, which is equivalent to a low frequency operation of cage induction machines, are the detrimental R_s effects leading to unwanted λ_s weakening and control degradation if the zero vectors are repeatedly applied at low u_s and ω_s values. For these reasons, they have not been employed with an incentive to facilitate the HPQC and retain its speed independence in either operating mode. Somewhat higher switching rates are clearly unavoidable to accommodate these conveniences, but this compromise is more than offset by the acquired performance boost.

The $\underline{\lambda}_s$, and thus P, dynamics depend on the flux instant position. For example, if $\underline{\lambda}_s$ is in sector 1 as shown in Fig. 4, applying either $\underline{u}_2$ or $\underline{u}_3$ to the BDFRM would shift $\underline{\lambda}_s$ anti-clockwise increasing both δ and $P > 0$ according to (4). With $\underline{\lambda}_m$ leading $\underline{\lambda}_s$ for the BDFRG, the same voltages would reduce δ but likewise increase $P < 0$ (i.e. less positive power produced by the primary) as in the BDFRM case when the power flow is reversed (negative). On the other hand, $\underline{u}_6$ or $\underline{u}_5$ have totally opposite effects on P to $\underline{u}_2$ or $\underline{u}_3$ regardless of the machine operating

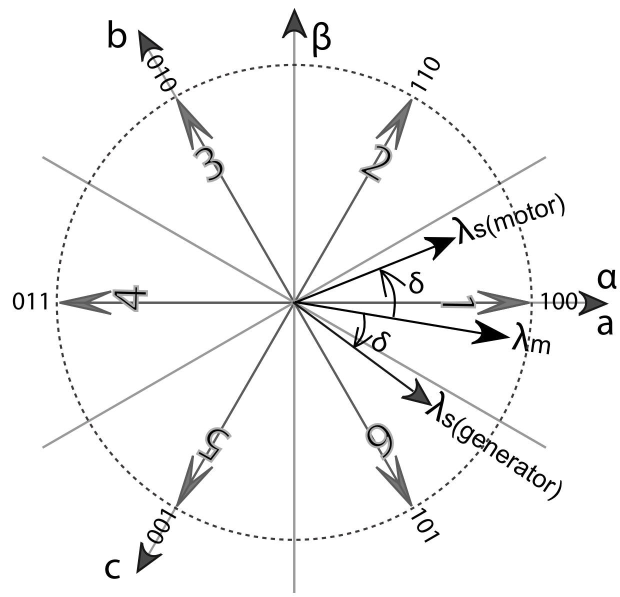

Figure 4: Active voltage vectors of two-level inverter fed secondary and respective 60° sectors in a stator plane.

regime. The voltage vectors to be applied to get the desired P increments for each individual $\underline{\lambda}_s$ sector in Fig. 4 are given in Table 1.

As already discussed, the Q control can be accomplished by varying λ_s. It can be seen from Fig. 4 that either $\underline{u}_1$, $\underline{u}_2$ or $\underline{u}_6$ would result in an increase of λ_{sd} (Fig. 2), and hence λ_s i.e. a decrease of Q. The impacts of $\underline{u}_3$, $\underline{u}_4$ or $\underline{u}_5$ would be such to ask for more Q from the grid, and are again the operating mode invariant as with the P control scenarios. The inverter voltages requested to meet the specific dQ demands for a given $\underline{\lambda}_s$ sectorial position can be found in Table 1 too.

3.2. Control procedure

A HPQC schematic is shown in Fig. 1. The P^* and Q^* set-points refer to the optimum performance indicators of interest to a particular application e.g. P^* for the maximum power point tracking (MPPT) and Q^* to get near unity power

Table 1: Secondary voltage effects on primary power differentials

$Sector \backslash Change$	$dP > 0$	$dP < 0$	$dQ > 0$	$dQ < 0$
1	$\underline{u}_2, \underline{u}_3$	$\underline{u}_6, \underline{u}_5$	$\underline{u}_5, \underline{u}_3, \underline{u}_4$	$\underline{u}_6, \underline{u}_1, \underline{u}_2$
2	$\underline{u}_3, \underline{u}_4$	$\underline{u}_1, \underline{u}_6$	$\underline{u}_6, \underline{u}_4, \underline{u}_5$	$\underline{u}_1, \underline{u}_2, \underline{u}_3$
3	$\underline{u}_4, \underline{u}_5$	$\underline{u}_2, \underline{u}_1$	$\underline{u}_1, \underline{u}_5, \underline{u}_6$	$\underline{u}_2, \underline{u}_3, \underline{u}_4$
4	$\underline{u}_5, \underline{u}_6$	$\underline{u}_3, \underline{u}_2$	$\underline{u}_2, \underline{u}_6, \underline{u}_1$	$\underline{u}_3, \underline{u}_4, \underline{u}_5$
5	$\underline{u}_6, \underline{u}_1$	$\underline{u}_4, \underline{u}_3$	$\underline{u}_3, \underline{u}_1, \underline{u}_2$	$\underline{u}_4, \underline{u}_5, \underline{u}_6$
6	$\underline{u}_1, \underline{u}_2$	$\underline{u}_5, \underline{u}_4$	$\underline{u}_4, \underline{u}_2, \underline{u}_3$	$\underline{u}_5, \underline{u}_6, \underline{u}_1$

factor (e.g. typically between 0.95 lagging and leading) for WECS [4]. The 3-phase power inputs to the hysteresis comparators are generated from the stationary $\alpha\beta$ components (Fig. 2) of the line current and voltage measurements for the Y-connected primary winding with an isolated neutral point and 'abc' phase sequence (Fig. 4) as follows:

$$\left.\begin{aligned} P &= \underbrace{i_a}_{i_\alpha} \cdot \underbrace{\frac{u_{ab}+u_{ac}}{2}}_{u_\alpha} + \underbrace{\frac{i_a+2i_b}{\sqrt{3}}}_{i_\beta} \cdot \underbrace{\frac{\sqrt{3}u_{bc}}{2}}_{u_\beta} \\ Q &= \underbrace{i_a}_{i_\alpha} \cdot \underbrace{\frac{\sqrt{3}u_{bc}}{2}}_{u_\beta} - \underbrace{\frac{i_a+2i_b}{\sqrt{3}}}_{i_\beta} \cdot \underbrace{\frac{u_{ab}+u_{ac}}{2}}_{u_\alpha} \end{aligned}\right\} \tag{6}$$

The integer error outputs from the comparators (Fig. 1), P_{err} and Q_{err}, and the secondary flux sector number (k) allow to retrieve the relevant inverter switching information from the look-up tables for a suitable secondary voltage vector to simultaneously satisfy the dP and dQ control specifications in line with Table 1 where the highlighted $\underline{u}_k$ and $\underline{u}_{k+3}$ vectors are not applicable. Implementing the switching logic as per the resulting Table 2 in the controller should make sure that the instantaneous P and Q values are kept within the user-defined hysteresis bands around the reference trajectories i.e. $[P^* - \delta P, P^* + \delta P]$ and $[Q^* - \delta Q, Q^* + \delta Q]$.

Table 2: Inverter switching vectors

$PowerDeviations$		$Sector(k)$					
$P^* - P$	$Q^* - Q$	1	2	3	4	5	6
$\leq -\delta P$	$> \delta Q$	$\underline{u}_5$	$\underline{u}_6$	$\underline{u}_1$	$\underline{u}_2$	$\underline{u}_3$	$\underline{u}_4$
$\leq -\delta P$	$\leq -\delta Q$	$\underline{u}_6$	$\underline{u}_1$	$\underline{u}_2$	$\underline{u}_3$	$\underline{u}_4$	$\underline{u}_5$
$> \delta P$	$> \delta Q$	$\underline{u}_3$	$\underline{u}_4$	$\underline{u}_5$	$\underline{u}_6$	$\underline{u}_1$	$\underline{u}_2$
$> \delta P$	$\leq -\delta Q$	$\underline{u}_2$	$\underline{u}_3$	$\underline{u}_4$	$\underline{u}_5$	$\underline{u}_6$	$\underline{u}_1$

Table 3: Anticipated ΔQ sign ($\pm$) | Flux sector increments (± 1)

k	$\underline{u}_1$	$\underline{u}_2$	$\underline{u}_3$	$\underline{u}_4$	$\underline{u}_5$	$\underline{u}_6$
1		$-\|-1$	$+\|+1$		$+\|-1$	$-\|+1$
2	$-\|+1$		$-\|-1$	$+\|+1$		$+\|-1$
3	$+\|-1$	$-\|+1$		$-\|-1$	$+\|+1$	
4		$+\|-1$	$-\|+1$		$-\|-1$	$+\|+1$
5	$+\|+1$		$+\|-1$	$-\|+1$		$-\|-1$
6	$-\|-1$	$+\|+1$		$+\|-1$	$-\|+1$	

3.3. Secondary flux sector ascertainment

One of the principal strengths of the proposed HPQC over DTC is a unique $\underline{\lambda}_s$ sector identification technique, which is not founded on the $\underline{\lambda}_s$ estimation or its absolute position knowledge, but on monitoring the measurable incremental changes of Q (ΔQ) instead. On these grounds, it is essentially indirect in principle and allows entirely parameter independent sensorless power control.

Commencing with the case study considered in Fig. 4 as an initial $\underline{\lambda}_s$ sector condition and looking at the possible voltage-sector combinations from Tables 2 and 3, if $\underline{u}_2$ or $\underline{u}_6$ are applied then $\Delta Q < 0$ (i.e. '-' in Table 3), else $\underline{u}_3$ or $\underline{u}_5$ are the secondary terminal voltages and $\Delta Q > 0$ (i.e. '+' in Table 3). So, as long as the predictions in the ΔQ sign (Table 3) are coincident with the calculations obtained from measurements using (6), no control action for the sector transition should be taken. Otherwise, any disagreement in the results may suggest that an unknown machine speed mode reliant sector change has occurred, and that the sector counter is to be updated by ± 1 as $\underline{\lambda}_s$ can't instantly 'jump' through the sectors. At super-synchronous speeds, the $\underline{\lambda}_s$ rotating counter-clockwise goes to sector 2 where $\underline{u}_3$ and $\underline{u}_6$ have completely different effects on ΔQ than in sector 1, causing a sudden alteration of the ΔQ sign and hence the sector number. Similarly, for sub-synchronous speed operation and clockwise rotation of $\underline{\lambda}_s$, $\underline{u}_2$ and $\underline{u}_5$ are the two pointing vectors to a sector change from 1 to 6.

4. Experimental verification

The HPQC scheme was implemented on a dSPACE® control prototyping platform of a custom-made test rig (Fig. 5) for a 6/2-pole BDFRG with both windings rated at 415 V, 2.5 A, 50 Hz. The two-level voltage source inverter is a Semikron® smart power IGBT module (Skiip®). A commercial four-quadrant Parker® DC drive emulated the chosen prime mover (e.g. wind turbine) characteristics of the BDFRG as explained in [36]. The remaining machine data and details of the apparatus used for testing can be found in [30]. The system sampling rate was 10 kHz, and the variable switching frequency was around 5 kHz. The hysteresis bands were set to $\delta P = 50$ W and $\delta Q = 100$ VAr.

The BDFRG is self-started as a wound rotor induction machine to the steady no-load speed (Fig. 6). The inverter was then enabled, and the HPQC viability proven by laboratory tests for three ordinary speed set-points in a narrow range down to synchronous speed for step-changes in P^* and/or Q^* settings. An incremental encoder was used for instrumentation purposes and to provide feedback to the DC drive to maintain the desired shaft speed externally as the prime objective

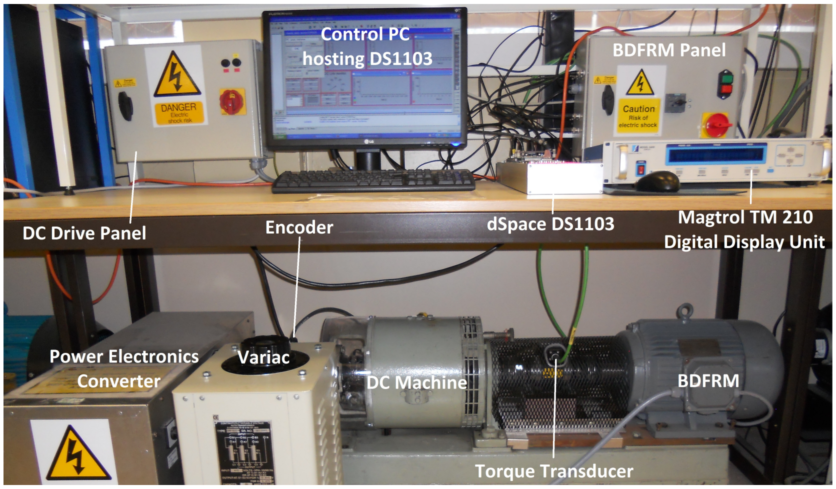

Figure 5: A photo of the BDFRG test facility used for experimental studies.

was to evaluate the algorithm in power mode. In a real WECS with HPQC, this sensor would only serve to generate the necessary P^* for MPPT [1] as depicted in Fig. 1. Sensorless MPPT options are also possible [37].

4.1. Open-loop speed control

The P step response in Fig. 7 demonstrates the high HPQC performance with a smooth and swift changeover from BDFRM to BDFRG operation. For instance, such mode reversals, whilst not so rapid, are encountered with reversible pump-turbine devices for load balancing in pumped-storage hydro-power plants [38, 39]. The corresponding Q trace shows little or no apparent signs of cross-coupling pertaining to this transition, such as level shifting or other steady-state disturbances. A short speed dip comes from the sudden load increase perceived by the DC machine when the BDFRG starts generating P. For a given Q^*, the primary current (i_a) is virtually unaffected by the P transient with its largely magnetizing nature,

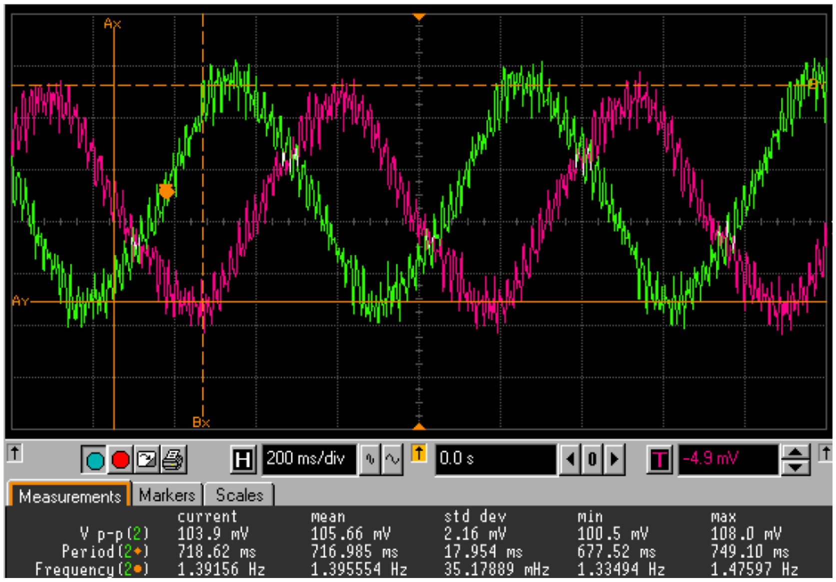

Figure 6: Oscillograms of the recorded steady-state currents in two phases of the shorted secondary winding for the unloaded BDFRG at $\approx$ 730 rev/min.

and hence the fairly uniform magnitudes throughout at line frequency[2]. However, the peak secondary currents (i_{s_a}), as predominantly torque producing, get higher to accommodate the rise of T_e and P_m required to cover the BDFRG losses in delivering the same P as consumed for the BDFRM operation. Moreover, from (2), the secondary frequency (f_s) should be -6.67 Hz at 650 rev/min, which can be found indeed true by counting $\approx$ 17 150 ms cycles over 2.5 s on the measured i_{s_a} waveform. The last graph in Fig. 7 shows the descending sector changes of the clockwise rotating $\underline{\lambda}_s$ as '$f_s < 0$' (Figs. 2 and 4).

The results in Fig. 8 are complementary to those in Fig. 7. The HPQC properties for a stepping-down Q^* and the 'idling' machine playing an inductive role are

[2]There are 25 sine waves, each of 20 ms in period (i.e. $f_p = 50$ Hz), over a 0.5 s time interval on the respective zoomed-in sub-plot of Fig. 7.

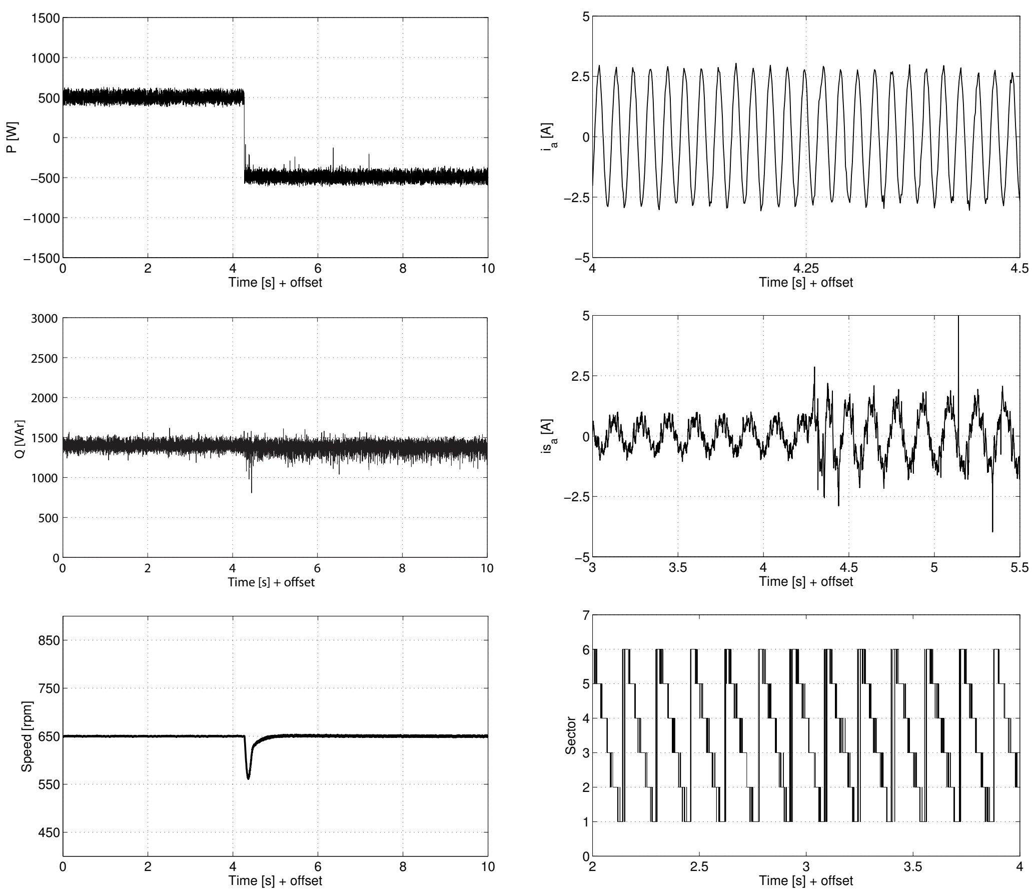

Figure 7: BDFRG(M) performance in sub-synchronous mode at 650 rev/min for $P^* = \pm$ 500 W and $Q^* = 1.35$ kVAr.

examined now. Albeit not practical, this is an extremely insightful and challenging scenario from a control perspective as the current in either winding is then mostly reactive allowing the effects of varying Q^* to be investigated separately from P. The power plots in Fig. 8 are another evidence of robust and decoupled control, although fast transients may be superfluous for the BDFRG target applications. Unlike Fig. 7, the shaft speed is barely influenced by the Q^* change as expected for an unloaded machine, whereas the i_a amplitudes exhibit a foreseen decline with the Q reduction. The magnetizing i_{s_a} will thus increase in magnitude in much the same manner as it does in Fig. 7.

The measurements in Fig. 9 reinforce the controller's ability to successfully track the stipulated Q^* trajectory, and its capacity to instantly react to an even doubled step-change of Q^* than in Fig. 8. More importantly, the mid P value doesn't seem to be impaired in any way by such a big Q perturbation. The i_a has notably decreased, and the i_{s_a}, taking over the machine magnetization from the primary winding increased, in magnitude nearly in the same proportion as the Q level has diminished with the power factor improvement indicating the mainly flux producing share of both the currents.

The majority of the HPQC observations and/or explanations of the physical phenomena behind the performance measures in Fig. 7 can be extended to those in Fig. 10. An exception is that the $\underline{\lambda}_s$ sector numbers are now in ascending order with the counter-clockwise rotation of the secondary vectors, which is contrary to the sub-synchronous case in Fig. 7. By analogy to the latter, the presence of ≈ 30 cycles on the i_{s_a} waveform in Fig. 10 during 4.5 s implies the same f_s of 6.67 Hz at 850 rev/min and 650 rev/min but with the opposite phase sequence (i.e. sign).

Much the same HPQC features can be discovered from Fig. 11. Either Q or P

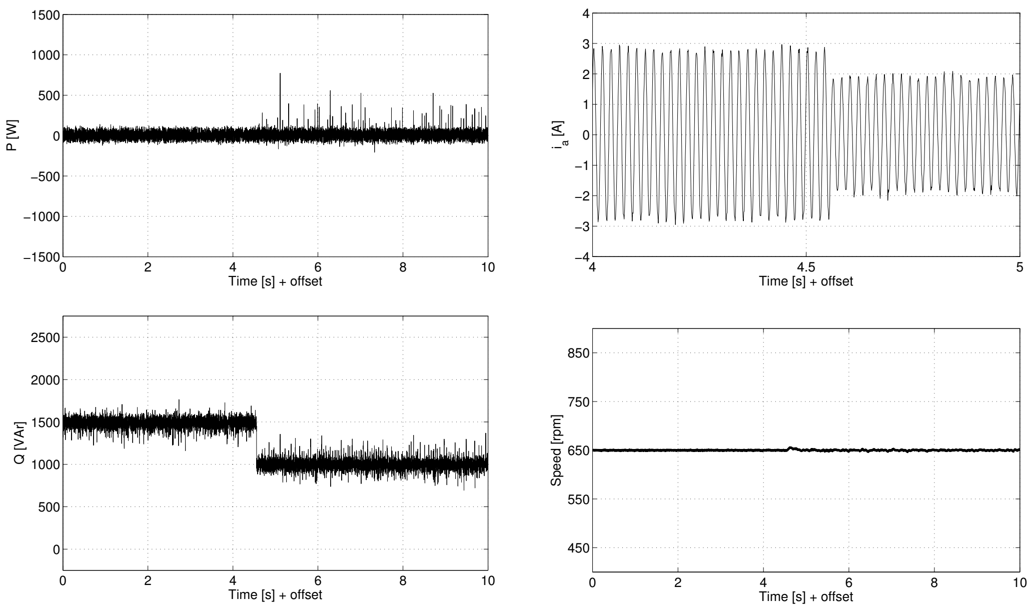

Figure 8: BDFRG sub-synchronous response to Q^* step change from 1.5 kVAr to 1 kVAr at 650 rev/min in 'stand-by' power mode (i.e. $P^* = 0$).

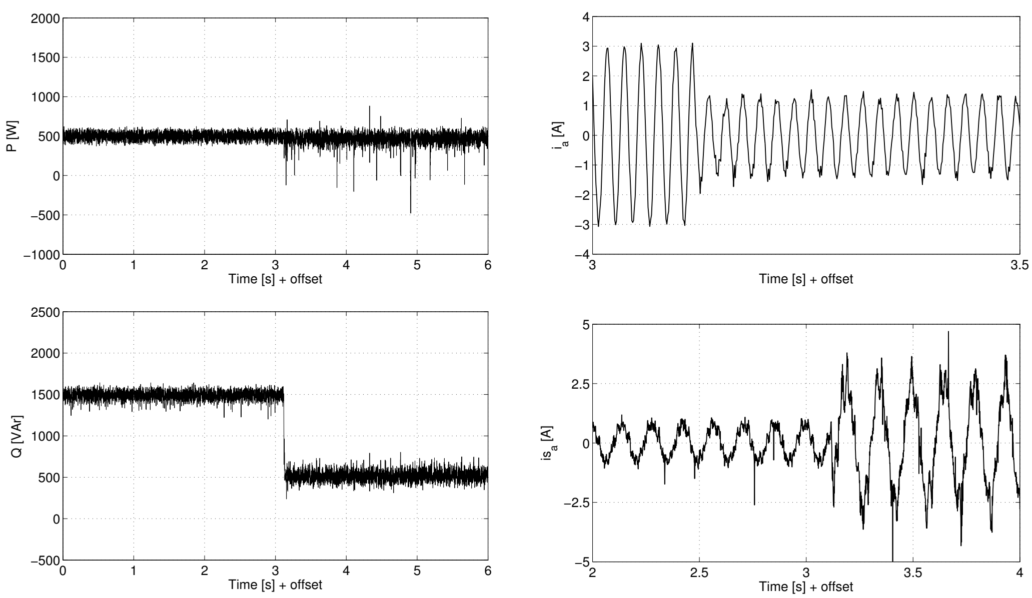

Figure 9: BDFRM response to a sudden Q^* drop from 1.5 kVAr to 500 VAr at 850 rev/min and $P^* = 500$ W in super-synchronous mode.

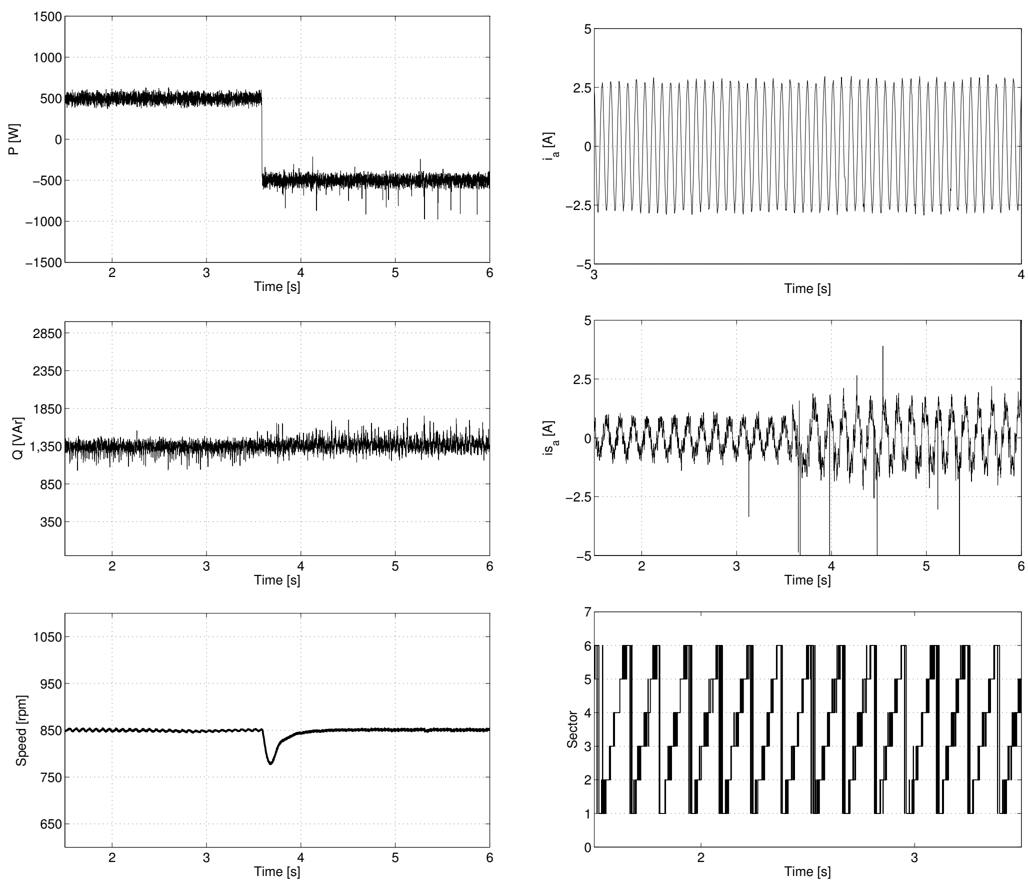

Figure 10: Super-synchronous operation of the BDFRG(M) at 850 rev/min, $P^* = \pm\, 500$ W and $Q^* = 1.35$ kVAr.

responses appear to be insensitive (in average terms) to the step-down change of P^* not experiencing any visible form of disruption. The speed glitch in Fig. 11 is less pronounced than in Fig. 7 because of the smaller P^* deviation to handle by the PI speed regulator of the DC drive.

4.2. Machine design vs performance trade-offs

Noise susceptibility and higher current ripples are common with hysteresis control by its 'bang-bang' complexion. This issue is more aggravated for the considered HPQC with the non-optimal design of the proof-of-concept BDFRG. The latest finite-element-analyses [40] have established the drawbacks of 6/2 pole winding arrangements with an axially-laminated rotor in terms of the presence of low-order harmonics and modest power density, identifying the 8/4 pole wound stators and modern radially-laminated ducted reluctance rotors as the way forward. The former limitation can clearly be attributed to our prototype judging by the visibly ripple-corrupted i_s waveforms even without switching power electronics in Fig. 6 and manifesting also in Figs. 7, 9 and 10 for the controlled machine. Similar distortions, though incomparably less pronounced with the weak magnetic coupling between the windings, can be seen in the much cleaner primary i_a currents but only at higher i_s levels in Fig. 9. Furthermore, the unusually large $R_s \approx 13\ \Omega$ contravenes the main HPQC assumption of negligible voltage drops causing modeling and control inaccuracies as $\underline{e}_s$, and not $\underline{u}_s$, dictates $d\underline{\lambda}_s/dt$ given (1). This is predominantly the case with increasing i_s amplitudes as can be seen in the spiky P, and foremost Q, responses (Figs. 7, 9 and 10) or at lower Q^* requirements (Figs. 8, 9 and 11). Finally, the secondary winding is not appropriately rated to accomplish close to unity primary power factor without tripping of the over-current protection.

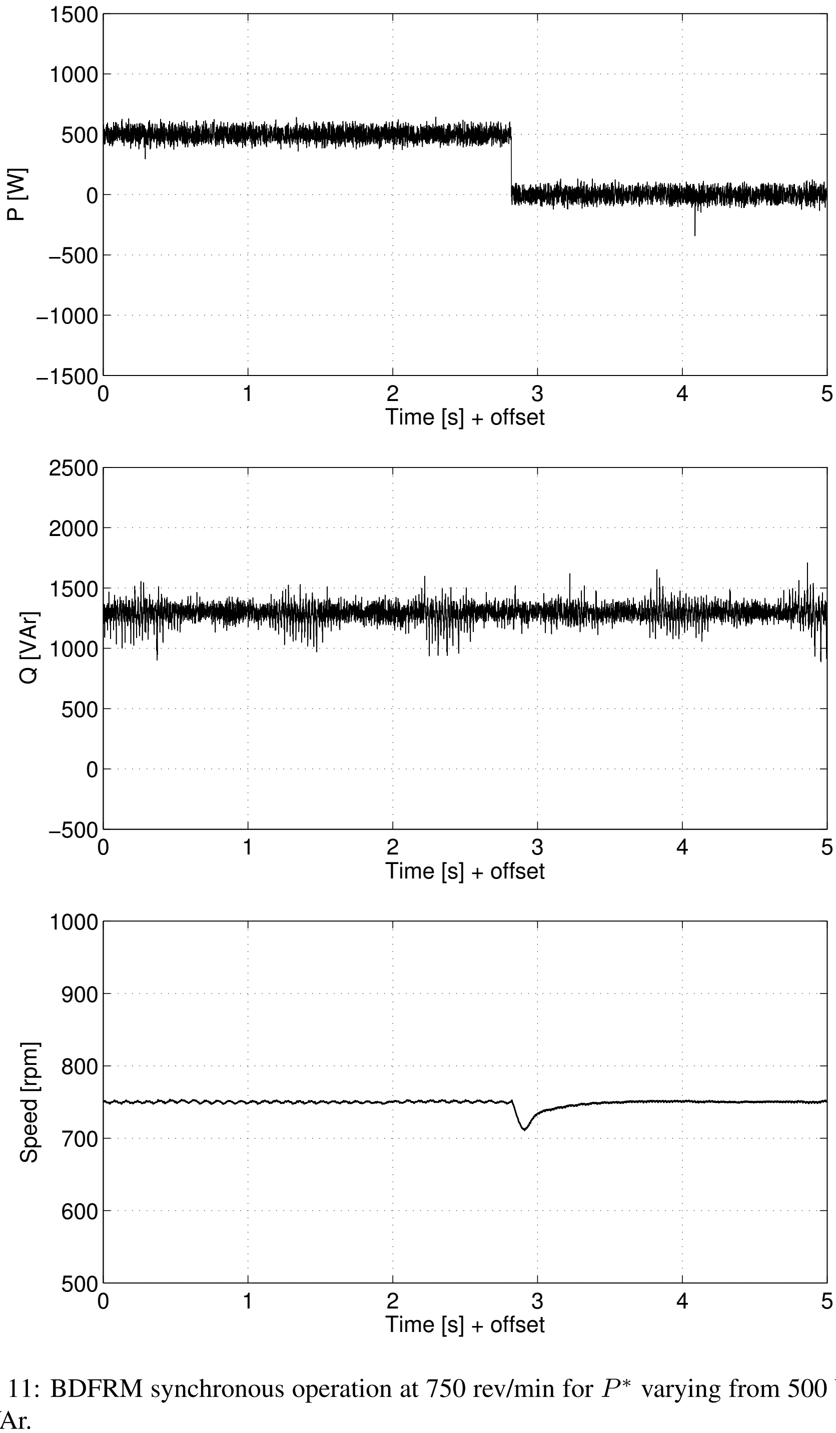

Figure 11: BDFRM synchronous operation at 750 rev/min for P^* varying from 500 W to 0 W at 1.3 kVAr.

5. Conclusions

A robust, machine parameter-free HPQC algorithm for the BDFRG has been suggested and successfully experimentally validated by the results presented. Originating from the basic electro-magnetic relationships for doubly-excited machines renders it versatile and potentially suitable to any member of this family. These virtues, coupled with the computational effectiveness and ease of implementation, offer superior performance to the existing DT(P)C methods and could strengthen the HPQC standing as a viable competitor of model-based or PI control strategies.

A good overall response and disturbance rejection abilities of both the P and Q sub-controllers have been verified on the early small-scale prototype despite the challenging test conditions imposed by its high winding resistances and crude design. The adverse resistive effects and control deterioration at low secondary voltages and frequencies over a narrow speed range have been mitigated by omitting the two zero-vectors in the inverter switching strategy being applied. The accompanying speed mode reliance and emanating complexities of the HPQC scheme, that would have been otherwise introduced, had been avoided as an added bonus. A significant performance enhancement would be envisaged with larger, more representative machines having much smaller resistances.

The above merits, along with the rotor position and velocity independence, form a basis for facilitated sensorless HPQC of WECS, or the use of a low to medium resolution sensor, as very accurate estimates or high-bandwidth measurements of the shaft speed are not imperative for MPPT in these applications. Finally, given the conceptual similarities with the DTC, the HPQC may draw attention of industrial companies like ABB with its existing production line of DTC power converters (e.g. the ACS800 series) for DFIG and other MW wind turbines.

References

[1] M. Cheng, Y. Zhu, The state of the art of wind energy conversion systems and technologies: A review, Energy Conversion and Management 88 (2014) 332–347.

[2] R. Cardenas, R. Pena, S. Alepuz, G. Asher, Overview of control systems for the operation of DFIGs in wind energy applications, IEEE Transactions on Industrial Electronics 60 (7) (2013) 2776–2798.

[3] J. Carroll, A. McDonald, D. McMillan, Reliability comparison of wind turbines with DFIG and PMG drive trains, IEEE Transactions on Energy Conversion 30 (2) (2015) 663–670.

[4] J. G. Njiri, D. Soffker, State-of-the-art in wind turbine control: Trends and challenges, Renewable and Sustainable Energy Reviews 60 (2016) 377–393.

[5] J. Mohammadi, S. Afsharnia, S. Vaez-Zadeh, Efficient fault-ride-through control strategy of DFIG-based wind turbines during the grid faults, Energy Conversion and Management 78 (2014) 88–95.

[6] S. Tohidi, P. Tavner, R. McMahon, H. Oraee, M. Zolghadri, S. Shao, E. Abdi, Low voltage ride-through of DFIG and brushless DFIG: Similarities and differences, Electric Power Systems Research 110 (2014) 64–72.

[7] A. Rahim, E. Nowicki, Supercapacitor energy storage system for fault ride-through of a DFIG wind generation system, Energy Conversion and Management 59 (2012) 96–102.

[8] K. Vinothkumar, M. Selvan, Novel scheme for enhancement of fault ride-through capability of doubly fed induction generator based wind farms, Energy Conversion and Management 52 (7) (2011) 2651–2658.

[9] S. Tohidi, B. Mohammadi-ivatloo, A comprehensive review of low voltage ride through of doubly fed induction wind generators, Renewable and Sustainable Energy Reviews 57 (2016) 412–419.

[10] H. Zeng, Y. Zhu, J. Liu, Verification of DFIG and PMSG wind turbines' LVRT characteristics through field testing, in: Power System Technology (POWERCON), 2012 IEEE International Conference on, 2012, pp. 1–6.

[11] A. Oraee, E. Abdi, S. Abdi, R. McMahon, P. Tavner, Effects of rotor winding structure on the BDFM equivalent circuit parameters, IEEE Transactions on Energy Conversion 30 (4) (2015) 1660–1669.

[12] A. Knight, R. Betz, D. Dorrell, Design and analysis of brushless doubly fed reluctance machines, IEEE Transactions on Industry Applications 49 (1) (2013) 50–58.

[13] E. Abdi, R. McMahon, P. Malliband, S. Shao, M. Mathekga, P. Tavner, S. Abdi, A. Oraee, T. Long, M. Tatlow, Performance analysis and testing of a 250 kW medium-speed brushless doubly-fed induction generator, IET Renewable Power Generation 7 (6) (2013) 631–638.

[14] F. Wang, F. Zhang, L. Xu, Parameter and performance comparison of doubly-fed brushless machine with cage and reluctance rotors, IEEE Transactions on Industry Applications 38 (5) (2002) 1237–1243.

[15] R. Zhao, A. Zhang, Y. Ma, X. Wang, J. Yan, Z. Ma, The dynamic control of reactive power for the brushless doubly fed induction machine with indirect stator-quantities control scheme, IEEE Transactions on Power Electronics 30 (9) (2015) 5046–5057.

[16] S. Abdeddaim, A. Betka, S. Drid, M. Becherif, Implementation of MRAC controller of a DFIG based variable speed grid connected wind turbine, Energy Conversion and Management 79 (2014) 281–288.

[17] J. Chen, W. Zhang, B. Chen, Y. Ma, Improved vector control of brushless doubly fed induction generator under unbalanced grid conditions for offshore wind power generation, IEEE Transactions on Energy Conversion 31 (1) (2016) 293–302.

[18] I. Sarasola, J. Poza, M. A. Rodriguez, G. Abad, Direct torque control design and experimental evaluation for the brushless doubly fed machine, Energy Conversion and Management 52 (2) (2011) 1226–1234.

[19] H. Chaal, M. Jovanovic, Toward a generic torque and reactive power controller for doubly fed machines, IEEE Transactions on Power Electronics 27 (1) (2012) 113–121.

[20] F. Zhang, L. Zhu, S. Jin, W. Cao, D. Wang, J. L. Kirtley, Developing a new SVPWM control strategy for open-winding brushless doubly fed reluctance generators, IEEE Transactions on Industry Applications 51 (6) (2015) 4567–4574.

[21] L. Xu, B. Guan, H. Liu, L. Gao, K. Tsai, Design and control of a high-efficiency doubly-fed brushless machine for wind power generator applica-

tion, in: 2010 IEEE Energy Conversion Congress and Exposition, 2010, pp. 2409–2416.

[22] D. G. Dorrell, M. Jovanović, On the possibilities of using a brushless doubly-fed reluctance generator in a 2 MW wind turbine, IEEE Industry Applications Society Annual Meeting (2008) 1–8.

[23] F. Valenciaga, Second order sliding power control for a variable speed-constant frequency energy conversion system, Energy Conversion and Management 52 (12) (2010) 3000–3008.

[24] M. G. Jovanović, J. Yu, E. Levi, Encoderless direct torque controller for limited speed range applications of brushless doubly fed reluctance motors, IEEE Transactions on Industry Applications 42 (3) (2006) 712–722.

[25] M. Jovanović, Sensored and sensorless speed control methods for brushless doubly fed reluctance motors, IET Electric Power Applications 3 (6) (2009) 503–513.

[26] H. Chaal, M. Jovanović, Practical implementation of sensorless torque and reactive power control of doubly fed machines, IEEE Transactions on Industrial Electronics 59 (6) (2012) 2645–2653.

[27] H. Chaal, M. Jovanovic, Power control of brushless doubly-fed reluctance drive and generator systems, Renewable Energy 37 (1) (2012) 419–425.

[28] S. Ademi, M. Jovanović, High-efficiency control of brushless doubly-fed machines for wind turbines and pump drives, Energy Conversion and Management 81 (2014) 120–132.

[29] S. Ademi, M. Jovanović, M. Hasan, Control of brushless doubly-fed reluctance generators for wind energy conversion systems, IEEE Transactions on Energy Conversion 30 (2) (2015) 596–604.

[30] S. Ademi, M. Jovanovic, Control of doubly-fed reluctance generators for wind power applications, Renewable Energy 85 (2016) 171–180.

[31] S. Ademi, M. Jovanovic, Control of emerging brushless doubly-fed reluctance wind turbine generators, in: J. Hossain, A. Mahmud (Eds.), Large Scale Renewable Power Generation, Green Energy and Technology, Springer Singapore, 2014, pp. 395–411.

[32] S. Ademi, M. G. Jovanović, H. Chaal, W. Cao, A new sensorless speed control scheme for doubly fed reluctance generators, IEEE Transactions on Energy Conversion 31 (3) (2016) 993–1001.

[33] S. Ademi, M. Jovanović, A novel sensorless speed controller design for doubly-fed reluctance wind turbine generators, Energy Conversion and Management 120 (2016) 229–237.

[34] S. Ademi, M. Jovanović, Vector control methods for brushless doubly fed reluctance machines, IEEE Transactions on Industrial Electronics 62 (1) (2015) 96–104.

[35] R. E. Betz, M. G. Jovanović, Introduction to the space vector modelling of the brushless doubly-fed reluctance machine, Electric Power Components and Systems 31 (8) (2003) 729–755.

[36] H. Camblong, I. M. de Alegria, M. Rodriguez, G. Abad, Experimental evaluation of wind turbines maximum power point tracking controllers, Energy Conversion and Management 47 (18-19) (2006) 2846–2858.

[37] W. Lin, C. Hong, F. Cheng, Design of intelligent controllers for wind generation system with sensorless maximum wind energy control, Energy Conversion and Management 52 (2) (2011) 1086–1096.

[38] J. I. Sarasúa, J. I. Pérez-Diaz, J. R. Wilhelmi, J. Ángel Sánchez-Fernández, Dynamic response and governor tuning of a long penstock pumped-storage hydropower plant equipped with a pump-turbine and a doubly fed induction generator, Energy Conversion and Management 106 (2015) 151–164.

[39] N. Sivakumar, D. Das, N. Padhy, Variable speed operation of reversible pump-turbines at Kadamparai pumped storage plant - a case study, Energy Conversion and Management 78 (2014) 96–104.

[40] T. Staudt, F. Wurtz, L. Gerbaud, N. J. Batistela, P. Kuo-Peng, An optimization-oriented sizing model for brushless doubly fed reluctance machines: Development and experimental validation, Electric Power Systems Research 132 (2016) 125–131.